

This item is likely protected under Title 17 of the U.S. Copyright Law. Unless on a Creative Commons license, for uses protected by Copyright Law, contact the copyright holder or the author.

Access to this work was provided by the University of Maryland, Baltimore County (UMBC) ScholarWorks@UMBC digital repository on the Maryland Shared Open Access (MD-SOAR) platform.

Please provide feedback

Please support the ScholarWorks@UMBC repository by emailing scholarworks-group@umbc.edu and telling us what having access to this work means to you and why it's important to you. Thank you.

SPECTRAL STATE DEPENDENCE OF THE 0.4–2 MEV POLARIZED EMISSION IN CYGNUS X-1 SEEN WITH *INTEGRAL*/IBIS, AND LINKS WITH THE AMI RADIO DATAJÉRÔME RODRIGUEZ¹, VICTORIA GRINBERG^{2,3}, PHILIPPE LAURENT⁴, MARION CADOLLE BEL⁵, KATJA POTTSCHMIDT^{6,7}, GUY POOLEY⁸, ARASH BODAGHEE⁹, JÖRN WILMS², AND CHRISTIAN GOUÏFFÈS¹¹ Laboratoire AIM, UMR 7158, CEA/DSM—CNRS—Université Paris Diderot, IRFU/SaP, F-91191 Gif-sur-Yvette, France; jrodriguez@cea.fr² Dr. Karl Remels-Sternwarte and Erlangen Centre for Astroparticle Physics, Friedrich Alexander Universität Erlangen-Nürnberg, Sternwartstr. 7, D-96049 Bamberg, Germany³ Massachusetts Institute of Technology, Kavli Institute for Astrophysics, Cambridge, MA 02139, USA⁴ Laboratoire APC, UMR 7164, CEA/DSM CNRS—Université Paris Diderot, Paris, France⁵ LMU, Excellence Cluster “Universe”, Boltzmannstrasse 2, D-85748 Garching, Germany⁶ CRESST, University of Maryland Baltimore County, 1000 Hilltop Circle, Baltimore, MD 21250, USA⁷ NASA Goddard Space Flight Center, Astrophysics Science Division, Code 661, Greenbelt, MD 20771, USA⁸ Astrophysics, Cavendish Laboratory, J J Thomson Avenue, Cambridge CB3 0HE, UK⁹ Georgia College & State University, Dept. of Chemistry, Physics, and Astronomy, CBX 82, Milledgeville, GA 31061, USA

Received 2014 February 26; accepted 2015 May 7; published 2015 June 25

ABSTRACT

Polarization of the $\gtrsim 400$ keV hard tail of the microquasar Cygnus X-1 has been independently reported by *INTEGRAL*/Imager on Board the *INTEGRAL* Satellite (IBIS), and *INTEGRAL*/Spectrometer on *INTEGRAL* and interpreted as emission from a compact jet. These conclusions were, however, based on the accumulation of all *INTEGRAL* data regardless of the spectral state. We utilize additional *INTEGRAL* exposure accumulated until 2012 December, and include the AMI/Ryle (15 GHz) radio data in our study. We separate the observations into hard, soft, and intermediate/transitional states and detect radio emission from a compact jet in hard and intermediate states (IS), but not in the soft. The 10–400 keV *INTEGRAL* (JEM-X and IBIS) state resolved spectra are well modeled with thermal Comptonization and reflection components. We detect a hard tail in the 0.4–2 MeV range for the hard state only. We extract the state dependent polarigrams of Cyg X-1, which are all compatible with no or an undetectable level of polarization except in the 400–2000 keV range in the hard state where the polarization fraction is $75\% \pm 32\%$ and the polarization angle $40^\circ 0' \pm 14^\circ 3'$. An upper limit on the 0.4–2 MeV soft state polarization fraction is 70%. Due to the short exposure, we obtain no meaningful constraint for the IS. The likely detection of a >400 keV polarized tail in the hard state, together with the simultaneous presence of a radio jet, reinforce the notion of a compact jet origin of the >400 keV emission.

Key words: accretion, accretion disks – black hole physics – stars: individual (Cyg X-1) – X-rays: stars

1. INTRODUCTION

Black hole binaries (BHB) transit through different “spectral states” during their outbursts. The two canonical ones are the soft state (also known as “high” state, hereafter HSS) and the hard state (also known as “low” state, hereafter LHS).

In the HSS, the emission is dominated by a bright and warm (~ 1 keV) accretion disk, the level of variability is low, and the power density spectrum is power-law like. Little or no radio emission is detected in this state, which is interpreted as evidence for an absence of jets.

In the LHS, the disk is colder (≤ 0.5 keV) and might be truncated at a large distance from the accretor (see however Reynolds & Miller 2013, for examples of results contradicting this picture). The X-ray spectrum shows a strong power-law like component extending up to hundreds of keV, usually with a roll-over at typically 50–200 keV. The level of rapid variability is higher than in the HSS and the power density spectrum shows a band limited noise component, sometimes with quasi-periodic oscillations (QPOs) with frequencies in the range ~ 0.1 –10 Hz. A so-called “compact jet” is detected mainly through its emission in the radio to infrared domain (e.g., Corbel et al. 2013) where the spectrum can be modeled by $F_\nu \propto \nu^{-\alpha}$ where $\alpha \leq 0$ up to a break frequency ν_{break} that usually lies in the infrared domain (Corbel & Fender 2002; Rahoui et al. 2011). Above this break, the spectrum is a typical synchrotron spectrum with $\alpha \geq 0.5$.

Intermediate states (IS) exist between the HSS and LH (see, e.g., Homan & Belloni 2005; Remillard & McClintock 2006; Fender et al. 2009, for reviews and more detailed state classifications). Transitions between states indicate drastic changes in the properties of the flows and thus are crucial for the understanding of accretion–ejection connection. During a transition from the LHS to the HSS, the compact jet is quenched (e.g., Fender et al. 1999; Coriat et al. 2011); discrete, sometimes superluminal ejections occur, the level of X-ray variability drops abruptly, and QPOs, if present in the given source, change types before disappearing (see, e.g., Varnière et al. 2011, 2012, and references therein for both a description of the different types of QPOs and a possible theoretical interpretation of their origin and link to the spectral states).

The BHB Cygnus X-1 (Cyg X-1) was discovered in 1964 (Bowyer et al. 1965). It is the first Galactic source known to host a black hole (Bolton 1975) as the primary, and recent estimates led to a black hole mass of $M_{\text{BH}} = 14.8 \pm 1.0 M_\odot$ (Orosz et al. 2011). The donor star is the O9.7 Iab star HDE 226868 (Bolton 1972; Walborn 1973) with $M_{\text{HDE}} = 19.2 \pm 1.9 M_\odot$ (Orosz et al. 2011).¹⁰ The system’s orbital period is 5.6 days (Webster & Murdin 1972; Brocksopp et al. 1999; Gies et al. 2003), it has an inclination $i = 27:1 \pm 0:8$ on the plane of the sky (Orosz et al. 2011),

¹⁰ See also Ziōłkowski (2014) who obtain somewhat different values.

and is located at a distance of $d = 1.86 \pm 0.12$ kpc from Earth (Reid et al. 2011; Xiang et al. 2011).

Cyg X-1 can be found in both the LHS and the HSS; up to 2010, it was predominantly in the LHS. Since then, the behavior has changed and it spends most of its time in the HSS (Grinberg et al. 2013). It sometimes undergoes partial (“failed”) transitions from the LHS to the HSS, and can be found in a transitional or intermediate state (e.g., Pottschmidt et al. 2003b). The detection of compact relativistic jets in the LHS (Stirling et al. 2001) places Cyg X-1 in the family of microquasars. It is one of the few microquasars known to have a hard tail extending to (and beyond) the MeV range (e.g., McConnell et al. 2000).

The presence of the MeV tail has recently been confirmed with the two main instruments onboard the ESA’s *INTEGRAL*: the Imager on Board the *INTEGRAL* Satellite (IBIS; Ubertini et al. 2003) and the SPectrometer on *INTEGRAL* (SPI; Vedrenne et al. 2003). Cadolle Bel et al. (2006) and Laurent et al. (2011, hereafter LRW11) detect it with IBIS, and Jourdain et al. (2012, hereafter JRC12) with SPI. Utilizing photons that Compton scattered in the upper plane of IBIS, (ISGRI; Lebrun et al. 2003), and are absorbed in its lower plane (PICsIT; Labanti et al. 2003, sensitive in the 200 keV–10 MeV energy band), we have shown that the ≥ 400 keV emission of Cyg X-1 was polarized at a level of about 70%. We obtained only a 20% upper limit on the degree of polarization at lower energies (LRW11). This result was independently confirmed by JRC12 using SPI data. Both studies obtained compatible results for the properties of the polarized emission, reinforcing the genuineness of this discovery. Both teams also suggested that the polarized emission was due to synchrotron emission coming from a compact jet.

The presence of polarized emission and the energy-dependency of the polarization have a profound implication on our understanding of accretion and ejection processes. It can help to distinguish between the different proposed emitting media (Comptonization corona versus synchrotron-self Compton jets) in microquasars and provide important clues to the composition, energetics and magnetic field of the jet.

A problem of both studies, however, is that they accumulated all *INTEGRAL* data available to them, regardless of the spectral state and radio (and thus jet) properties of the source. In this paper, we separate the whole *INTEGRAL* data set (accumulated up to 2012 December) into different spectral states and study the properties of the state resolved broad band 10–2000 keV emission of Cyg X-1. We also utilize the Ryle/AMI radio data to determine the state dependent level of 15 GHz jet emission. In Section 2, we describe the data reduction and in particular the so-called “Compton mode” that allowed us to discover and measure the polarization in Cyg X-1 (LRW11). We carefully separate the data into spectral states following a procedure based on the classification of Grinberg et al. (2013) that is described in Section 3. The results of both, the long term 15 GHz radio monitoring and *INTEGRAL* state resolved analysis, are presented in Section 4. We discuss the implications of our analysis in Section 5 and summarize our results in Section 6.

2. OBSERVATIONS AND DATA REDUCTION

2.1. Standard Data Reduction of the JEM-X and IBIS/ISGRI Data

Cyg X-1 has been extensively observed by *INTEGRAL* since the launch of the satellite; preliminary results of the very first observations are described by Pottschmidt et al. (2003a). In LRW11, we first considered all uninterrupted *INTEGRAL* pointings, also called “science windows” (ScWs), where Cyg X-1 had an offset angle of less than 10° from the center of the field of view. We then removed all ScWs from the performance verification phase so that our analysis covered the period from 2003 March 24 (MJD 52722, satellite revolution (rev.) 54) to 2010 June 26 (MJD 55369, rev. 938). We further excluded ScWs with less than 1000 s of good ISGRI and PICsIT time. This resulted in a total of 2098 ScWs. Polarization was detected when stacking this sample (LRW11).

In the present work, we added to the LRW11 sample all observations belonging to our Cyg X-1 *INTEGRAL* monitoring program (PI J. Wilms) made until 2012 December 28 (MJD 56289.8, rev. 1246). We applied the same filtering criteria to select good ScWs. We consider both the data of the low energy detector of IBIS, ISGRI (Lebrun et al. 2003), and of the X-ray monitors JEM-X (Lund et al. 2003). ISGRI is sensitive in the ~ 18 –1000 keV energy range, although its response falls off rapidly above a few hundred keV. The two JEM-X units cover the soft X-ray (3–30 keV) band. All data were reduced with the Off Line Scientific Analysis (OSA) v.10.0 software suite and the associated updated calibration (Caballero et al. 2012), following the methods outlined by Rodriguez et al. (2008b).

The brightest and most active sources of the field, Cyg X-1, Cyg X-2, Cyg X-3, 3A 1954+319, and EXO 2032+375, were subsequently taken into account in the extraction of spectra and light curves. The Cyg X-1 spectra of each ScW were extracted with 67 spectral channels. All ScWs belonging to the same state were then averaged to produce one ISGRI spectrum for each spectral state. The spectral classification is described in Section 3 (see Grinberg et al. 2013 for details of the method). A systematic error of 1% was applied for all spectral channels. Low significance channels were rebinned when necessary.

The JEM-X telescopes have a much smaller field of view than IBIS. The number of ScWs during which Cyg X-1 can be seen by these instruments is therefore smaller. Since rev. 983 (MJD 55501) both units are on for all observations. Before rev. 983, both units were used alternately, so that the number of ScWs and time coverage is not the same. We derived images and spectra in the standard manner following the cookbook, separating the data into states following the same criteria as for the IBIS data. We applied systematic errors of 2% to all spectral channels of both units.

2.2. The Compton Mode

Thanks to its two position-sensitive detectors ISGRI and PICsIT, IBIS can be used as a Compton polarimeter (Lei et al. 1997). The concept behind a Compton polarimeter utilizes the polarization dependence of the differential cross section for Compton scattering,

$$\frac{d\sigma}{d\Omega} = \frac{r_0^2}{2} \left(\frac{E'}{E_0} \right)^2 \left(\frac{E'}{E_0} + \frac{E_0}{E'} - 2 \sin^2 \theta \cos^2 \phi \right) \quad (1)$$

where r_0 is the classical electron radius, E_0 the energy of the incident photon, E' the energy of the scattered photon, θ the scattering angle, and ϕ the azimuthal angle relative to the polarization direction. Linearly polarized photons scatter preferentially perpendicularly to the incident polarization vector. Hence by examining the scattering angle distribution of the detected photons (also referred to as polarigrams)

$$N(\phi) = S \left[1 + a_0 \cos(2(\phi - \phi_0)) \right] \quad (2)$$

where S is the mean count rate, one can derive the polarization angle PA and polarization fraction Π . With $\text{PA} = \phi_0 - \pi/2 + n\pi$, Equation (2) becomes $N(\phi) = S[1 - a_0 \cos(2(\phi - \text{PA}))][2\pi]$. The polarization angle therefore corresponds to the minimum of $N(\phi)$. The polarization fraction is $\Pi = a_0/a_{100}$, where a_{100} is the amplitude expected for a 100% polarized source, obtained from Monte-Carlo simulations of the instrument. Forot et al. (2008) obtained $a_{100} = 0.30 \pm 0.02$, hence a $\sim 6.7\%$ systematics uncertainty that should be taken into account in the derivation of Π . Recent simulations allowed us to reduce the uncertainty on a_{100} to $\sim 3\%$ which is small compared to the statistical errors on $N(\phi)$ (see below), and is therefore neglected.

To measure $N(\phi)$, we followed the procedure described by Forot et al. (2008) that led to the successful detection of the polarized signal from the Crab Nebula. We consider events that interacted once in ISGRI and once in PICsIT. These events are automatically selected on board through a time coincidence algorithm. The maximum allowed time window was set to $3.8 \mu\text{s}$ during our observations. To derive the source flux as a function of ϕ , the Compton photons were accumulated in 6 angular bins, each with a width of 30° in azimuthal scattering angle. To improve the signal-to-noise ratio in each bin, we took advantage of the π symmetry of the differential cross section (Equation (2)), i.e., the first bin contains the photons with $0^\circ \leq \phi < 30^\circ$ and $180^\circ \leq \phi < 210^\circ$, etc. Chance coincidences, i.e., photons interacting in both detectors, but not related to a Compton event, were subtracted from each detector image following the procedure described by Forot et al. (2008). The derived detector images were then deconvolved to obtain sky images. The flux of the source in each ϕ bin was then measured by fitting the instrumental point-spread function to the source peak in the sky image.

The uncertainty of $N(\phi)$ is dominated by statistic fluctuations in our observations that are background dominated. Confidence intervals on a_0 and ϕ_0 are not derived by a $N(\phi)$ fit to the data, but through a Bayesian approach following Forot et al. (2008), based on the work presented in Vaillancourt (2006). The applicability of this method was recently thoroughly discussed in Maier et al. (2014). In this computation, we suppose that all real polarization angles and fractions have a uniform probability distribution (non-informative prior densities; Quinn 2012; Maier et al. 2014) and that the real polarization angle and fraction are ϕ_0 and a_0 . We then need the probability density distribution of measuring a and ϕ from N_{pt} independent data points in $N(\phi)$ over a period π , based on Gaussian distributions for the orthogonal Stokes components (Vaillancourt 2006; Forot et al. 2008; Maier

et al. 2014):

$$dP(a, \phi) = \frac{N_{\text{pt}} S^2}{\pi \sigma_S^2} \exp \left[-\frac{N_{\text{pt}} S^2}{2 \sigma_S^2} \left[a^2 + a_0^2 - 2aa_0 \cos(2\phi - 2\phi_0) \right] \right] a da d\phi \quad (3)$$

where σ_S is the uncertainty of S . Credibility intervals of a and ϕ correspond to the intervals comprised between the minimum and maximum values of the parameter considered in the two-dimensional 1σ contour plot (not shown).

3. THE SPECTRAL STATES OF CYG X-1

We previously developed a method to classify the states of Cyg X-1 at any given time based on hardness and intensity measurements with the *RXTE*/ASM and MAXI and on the hard X-ray flux obtained with the *Swift*/BAT (Grinberg et al. 2013). The ASM and MAXI data can be used to separate all three states (LHS, IS, HSS), while using BAT we can only separate the HSS, but not the LHS and IS from each other.

In microquasars in general and Cyg X-1 in particular, spectral transitions can occur on short timescales (hours; e.g., Böck et al. 2011). We thus performed the spectral classification for each individual ScW. This is a sufficiently small exposure over which to consider the source to be spectrally stable in the majority of the data. The IBIS 18–25 keV light curve is shown in Figure 1, where the different symbols and colors represent the three different spectral states.

Where available, we used simultaneous ASM data for the state classification. ScWs with two simultaneous ASM measurements that are classified into different states are presumed to have occurred during a state transition and are excluded from the analysis. Most ScWs are, however, not strictly simultaneous with any ASM measurements. To classify ScWs without simultaneous ASM measurements, we therefore used the closest ASM measurement within 6 hr before or after a given ScW. For the remaining pointings where no such ASM measurements exist, we used the same approach, first based on MAXI and then, if necessary, based on BAT. As shown by Grinberg et al. (2013), the probability that a state is wrongly assigned using this method is 5% within 6 hr of an ASM pointing for both the LHS and HSS, and $\sim 25\%$ for the IS.

Out of the 3302 IBIS ScWs, 1739 ($\sim 52.7\%$) were taken during the LHS, 868 ($\sim 26.3\%$) during the HSS and 316 ($\sim 9.6\%$) during the IS. The remaining 379 (11.5%) have an uncertain classification and are thus not considered in our analysis: 351 lack a simultaneous or quasi-simultaneous all sky monitor measurements that would allow a classification and 28 were caught during a state transition.

From MJD 55700 until MJD 56000, Cyg X-1 was highly variable and underwent several transitions on short timescales (particularly striking in Figure 1 of Grinberg et al. 2014). Inspection of some of the ScWs during this period shows that the source flux was very low in the ISGRI range. Since these ScWs were taken close to or in between state transitions, they were also removed from our analysis in order to limit the potential uncertainties they could introduce into the final data products. This filtering removed 32 additional ScWs.

The resulting IBIS exposure times are 2.05 Ms, 1.21 Ms, and 0.22 Ms for the LHS, HSS, and IS, respectively. The IBIS

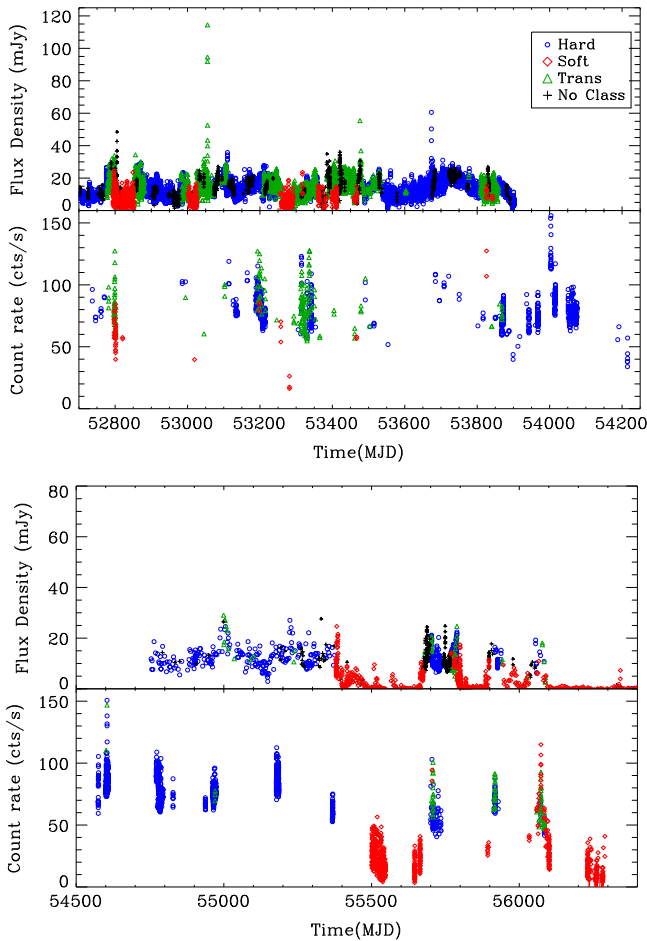


Figure 1. Two plots representing the long term radio (15 GHz, upper panels) *INTEGRAL*/IBIS hard X-ray (18–25 keV) light curves (lower panels) of Cyg X-1. The different symbols and colors indicate the different states of the source according to the classification presented by Grinberg et al. (2013). The upper plot covers the period MJD 52760–54250, when the radio monitoring was made with the older implementation of the radio telescope (known as the Ryle telescope). The lower one covers MJD 54500–56800 and shows the radio monitoring made after the upgrade (AMI telescope). Note the different vertical scales for the radio fluxes between the two plots.

18–25 keV and Ryle/AMI 15 GHz light curves are shown in Figure 1.

4. RESULTS

4.1. Radio Monitoring with the Ryle-AMI Telescope

The 2002–2012 15 GHz light curve classified utilizing the same method as for the *INTEGRAL* data is shown in Figure 1. As known from previous studies of microquasars, including Cyg X-1, the LHS and the IS show a high level of radio activity, while the radio flux is at a level compatible with or very close to zero during the soft state (e.g., Corbel et al. 2003; Gallo et al. 2003).

Cyg X-1 shows a high level of radio variability with a mean flux $\langle F_{15 \text{ GHz}} \rangle \sim 12 \text{ mJy}$ and flares. The most prominent flare occurred on MJD 53055 (2004 February 20) and reached a flux of 114 mJy.¹¹ Flares occur frequently (Figure 1), and are

connected with the X-ray behavior of the source (Fender et al. 2006; Wilms et al. 2007). The main flares seem to mostly coincide with the IS. The radio behavior in the LHS is usually steadier (although there is, e.g., a flare at MJD 53700, Figure 1).

We obtained state resolved mean radio fluxes of $\langle F_{15 \text{ GHz, LHS}} \rangle = 13.5 \text{ mJy}$, $\langle F_{15 \text{ GHz, IS}} \rangle = 15.4 \text{ mJy}$, and $\langle F_{15 \text{ GHz, HSS}} \rangle = 4.6 \text{ mJy}$. Given the typical rms uncertainty of $\text{rms}(5 \text{ minutes}) = 3.0 \text{ mJy}$ (e.g., Pooley & Fender 1997; Rodriguez et al. 2008a), the mean radio flux in the HSS is not detected at the 3σ level. The few clear radio detections in this state (Figure 1) do not correspond to a steady level of emission that would indicate a compact radio core (see also Fender et al. 1999). Such detections preferably occur after radio flares and thus likely represent the relic emission of previously ejected material (e.g., Corbel et al. 2004).

4.2. State Resolved Spectral Analysis

We analyzed the state resolved energy spectra of each instrument using XSPEC v.12.8.0 (Arnaud 1996). For JEM-X we considered the 10–20 keV range¹² and 20–400 keV for the ISGRI data. We used Compton data between 300 keV and 1 or 2 MeV, depending on their statistical quality. We started by fitting the spectra in the 10–400 keV range since the contribution of the 1 MeV power-law tail is supposed to be negligible here (LRW11). When an appropriate model was found for this restricted range, we added the 0.3–2 MeV Compton spectra and repeated the spectral analysis.

In order to find the most appropriate models describing the 10–400 keV spectra for all three spectral states, we proceeded in an incremental way. We started with a simple power-law model and added spectral model components until an acceptable fit according to χ^2 statistics was found. The phenomenological models were then replaced by more physical Comptonization models. Since the $\geq 10 \text{ keV}$ data are not affected by the absorption column density of $N_{\text{H}} \sim a \text{ few } 10^{22} \text{ cm}^{-2}$ (e.g., Böck et al. 2011; Grinberg et al. 2015), no modeling of the foreground absorption is necessary. Cross-calibration uncertainties and source variability during different exposure times are taken into account by a normalization constant. The ISGRI constant was frozen to one and the others left free to vary independently. We required that the values of the free constants were in the range [0.85, 1.15]. The best-fit parameters obtained with the best phenomenological and with the Comptonization models are reported in Table 1 for all three spectral states.

4.2.1. Hard state

A power law (Figure 2(a)) gives a very poor representation of the 10–400 keV data with a reduced $\chi^2 = \chi^2_\nu \sim 70$ for 87 degrees of freedom (dof). The broadband spectrum clearly departs from a straight line, which indicates a curved spectrum. A power law modified by a high energy cutoff (highcut* + power in XSPEC) provides a highly significant improvement with $\chi^2_\nu = 0.89$ for 85 dof (Figure 2(b)). We note, however,

¹¹ This flare was studied in detail by Fender et al. (2006), although the time axis of their Figure 4 is wrongly associated with MJD 55049.2–55049.6.

¹² Although the JEM-X units are well calibrated above $\sim 5 \text{ keV}$, we chose to ignore the lower energy bins. Due to the possible influence of a disk and presence of iron fluorescence line at 6.4 keV they would add uncertainties and degeneracies to the models that the low energy resolution does not allow us to constrain.

Table 1
Spectral Parameters of Fit to the 10–400 keV Spectra

reflect*highcut (powerlaw)						
State	Γ	E_{cut} (keV)	E_{fold} (keV)	10–20 keV	Fluxes ^b 20–200 keV	200–400 keV
LHS	1.43 ± 0.01	≤ 12	155 ± 4	4.48 ± 0.02	22.30 ± 0.03	3.56 ± 0.03
IS	$1.87^{+0.02}_{-0.03}$	56^{+4}_{-6}	198 ± 8	5.10 ± 0.03	18.47 ± 0.04	2.52 ± 0.05
HSS ^a	2.447 ± 0.007	130^{+11}_{-16}	198^{+135}_{-59}	1.83 ± 0.01	3.33 ± 0.01	0.18 ± 0.03
reflect*comptt						
State	$\Omega/2\pi$	kT_e (keV)	τ	10–20 keV	Fluxes ^b 20–200 keV	200–400 keV
LHS	0.13 ± 0.02	$59.4^{+1.3}_{-1.2}$	1.06 ± 0.03	4.37 ± 0.03	22.60 ± 0.03	3.70 ± 0.03
IS	0.04 ± 0.03	$54.4^{+3.6}_{-2.8}$	0.82 ± 0.06	5.30 ± 0.03	18.42 ± 0.06	1.93 ± 0.07
HSS	0.36 ± 0.03	279 ± 15	<0.013	1.84 ± 0.09	3.7 ± 0.6	0.36 ± 0.01

Notes. Errors and limits on the spectral parameters are given at the 90% confidence level, while the errors on the fluxes are at the 68% level.

^a A reflection component with $\Omega/2\pi = 0.46 \pm 0.04$ was included for a good spectral fit to be obtained.

^b In units of $10^{-9} \text{ erg cm}^{-2} \text{ s}^{-1}$.

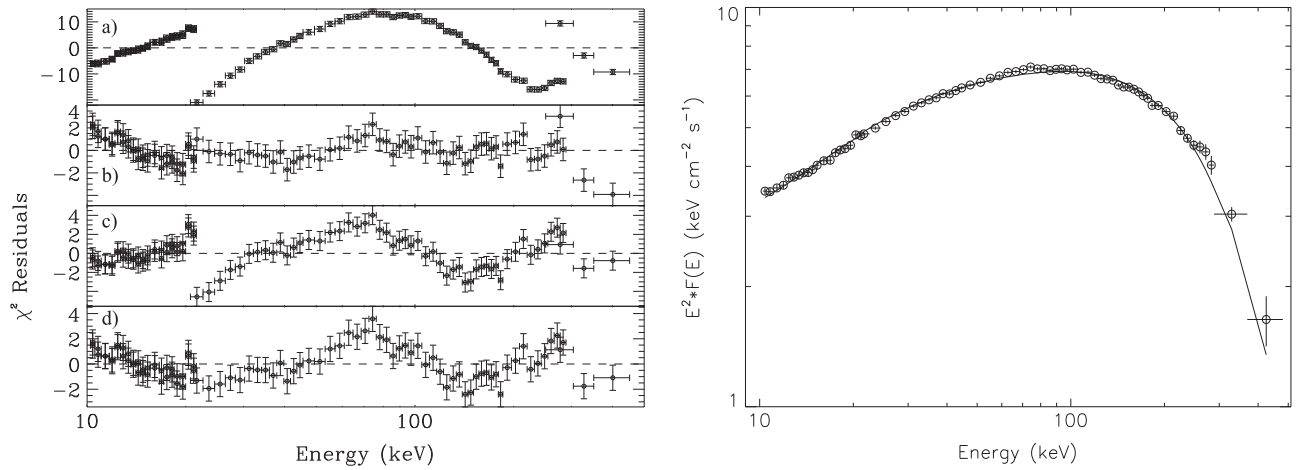


Figure 2. Left: χ^2 residuals to the hard state 10–400 keV spectra. From (a)–(d): simple power law, power law with an exponential cutoff, Comptonization, Comptonization convolved by a reflection model. Right: 10–500 keV $\nu - F_\nu$ (JEM-X+ISGRI) spectrum with the best model (Comptonization convolved by a reflection model) superimposed as a continuous line. For the sake of clarity only one JEM X spectrum is represented.

that the value of the high energy cutoff is unconstrained (Table 1), and deviations are seen at high energies.

As a cutoff power law in this energy range is usually assumed to mimic the spectral shape produced by an inverse Compton process, we replaced the phenomenological model by a more physical model *comptt* (Titarchuk 1994; Titarchuk & Hua 1995; Titarchuk & Lyubarskij 1995). Due to our comparably high lower energy bound, the temperature of the seed photons could not be constrained. We fix it to a typical LHS value of 0.2 keV (Wilms et al. 2006). Although the high energy part is better represented, the fit is statistically unacceptable ($\chi_\nu^2 = 2.9$ for 88 dof, Figure 2(c)) and significant residuals are visible in 10–80 keV range. In this range, hard X-ray photons can undergo reflection on the accretion disk. This effect is usually seen as an extra curvature, or bump in the 10–100 keV range in the spectra of microquasars and AGNs (García et al. 2014 and references therein). We thus included a simple reflection model (*reflect*) convolved with the Comptonization spectrum

and fixed the inclination angle to 30° . The residuals are much smaller, yielding an acceptable fit ($\chi_\nu^2 = 1.67$ for 87 dof).¹³ The normalization constants are 0.99, 1.06, and 0.98 for JEM X-1, JEM X-2, and the Compton mode respectively. The best fit results of this model are listed in Table 1, while the νF_ν broad band 10–400 keV spectrum is shown in the rightmost panel of Figure 2.

Next, we added the ≥ 400 keV Compton mode spectrum (Figure 3) to our data. These points are significant at the 8.2σ , 7.8σ , 6.9σ , and 6.5σ levels in the 451.4–551.9 keV, 551.9–706 keV, 706–1000.8 keV, and ~ 1 –2 MeV energy

¹³ We have followed the recommendations of the IBIS user manual regarding the level of systematics added to the IBIS spectral points (http://isdc.unige.ch/integral/download/osa/doc/10.0/osa_um_ibis/node74.html). Systematic errors of 1% seem to underestimate the real uncertainties when dealing with (large) data sets that encompass several calibration periods. We have tested this notion by refitting the spectra with 1.5% and 2% systematics and, as expected, obtain χ_ν^2 much closer to 1. Since the values of the spectral parameters, and thus the conclusions presented here, do not change significantly, we decided to present the spectral fits using the recommended 1% for systematics.

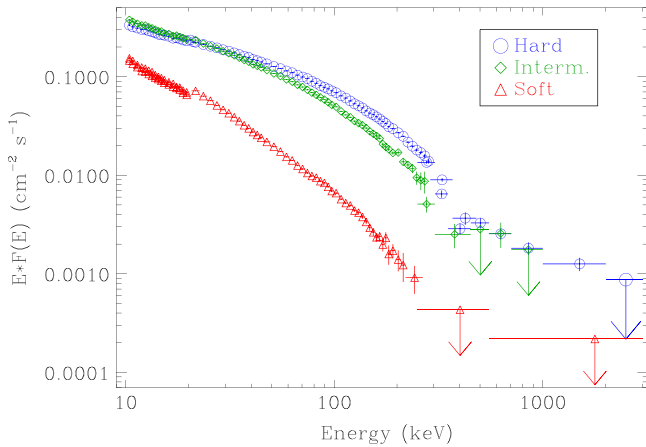


Figure 3. Unfolded 10 keV–2 MeV *INTEGRAL* spectra of Cyg X-1 in the three spectral states. The LHS spectrum is in blue circles, the IS in green diamonds and the HSS in red triangles.

bands. A significant deviation from the previous best fit model is clearly visible above 400 keV. An additional power law improves the fit significantly ($\chi^2_\nu = 1.4$ for 90 dof). The photon index of this additional power law is hard ($\Gamma = 1.1^{+0.3}_{-0.4}$) and marginally compatible with the values reported earlier (1.6 ± 0.2 , [LRW11](#)).

We model the reflection component using several distinct approaches, assuming (1) that the power-law component undergoes the same reflection as the Comptonization component (`reflect*(power+comptt)`), (2) that both components undergo reflection but with different solid angles $\Omega/2\pi$ (`reflect1*(power)+reflect2*(comptt)`), and (3) that the power law is not reflected (`power+reflect*(comptt)`). In model 2, the value for the reflection of the power-law component is unconstrained. Model 3 results in a better χ^2_ν , but the value of the power-law parameters are physically not acceptable. The normalization is too high and Γ too soft to reproduce the Compton data well. We therefore discard model 3, and consider model 1 as the most valid one. The value of the fit statistics is, however, still high with $\chi^2_\nu = 1.8$ for 89 dof. The residuals show deviations in the ~ 50 –200 keV range that may be due to the accumulation of a large set of ScWs taken at different calibration epochs and at different off-axis and roll angles of Cyg X-1.

In the final fit to the 10 keV–2 MeV broad band spectrum the parameters of the Comptonized component are $kT_e = 53 \pm 2$ keV and $\tau = 1.15 \pm 0.04$, the reflection fraction is unchanged, and the photon index of the hard tail is $\Gamma = 1.4^{+0.2}_{-0.3}$, i.e., essentially compatible with the value reported in [LRW11](#). The 0.4–1 MeV flux of the hard tail ($F_{\text{pow}, 0.4-1 \text{ MeV}} = 1.9 \times 10^{-9} \text{ erg cm}^{-2} \text{ s}^{-1}$) accounts for 86% of the total 0.4–1 MeV flux.

4.2.2. Intermediate State

A simple power law gives a poor representation of the IS spectrum ($\chi^2_\nu \sim 28$ for 82 dof). The inclusion of a high energy cutoff again greatly improves the fit ($\chi^2_\nu = 1.35$, 80 dof), but the normalization constant of the Compton spectrum (C_{Compton}) is outside the range that is consistent with the flux calibration of the instrument. Replacing the phenomenological model with a

`comptt` model, with the seed photon temperature fixed at 0.8 keV¹⁴ leads to a good fit ($\chi^2_\nu = 1.1$ for 81 dof) and a physical value of C_{Compton} . Although the statistics are not as good as in the LHS due to the much shorter total exposure, and the residuals in the 10–100 keV region are rather acceptable, we included a reflection component to be consistent with the LHS modeling. This approach improved the fit to $\chi^2_\nu = 0.97$ for 79 dof, which indicates a chance improvement of $\sim 1.2\%$ according to an F-test (the reflection component has a significance lower than 3σ). The reflection fraction is very low and poorly constrained ($\Omega/2\pi = 0.04 \pm 0.03$). As the other parameters are not significantly affected, we still report the results obtained with the latter model in Table 1 despite this weak evidence for reflection.

We then added the ≥ 400 keV spectral points of the Compton mode spectrum (Figure 3). The previous model (without reflection) leads to a good representation ($\chi^2_\nu = 1.2$ for 83 dof), even if a deviation at high energies is present. Above 400 keV, however, only the 551.9–706 keV Compton mode spectral point is significant at $\geq 3\sigma$. Adding a power law to the data leads to $\chi^2_\nu = 1.04$ (81 dof), which corresponds to a chance improvement of 0.1%. Not surprisingly, the power-law photon index Γ is poorly constrained ($-0.4 \leq \Gamma \leq 1.8$) and the normalization constant for the Compton mode spectral points C_{Compton} tends to be a very low value if not forced to be above 0.85. Fixing Γ at 1.6 ([LRW11](#), [JRC12](#)) and setting C_{Compton} to 0.90, the best value found in the LHS fits, allows us to estimate a 3σ upper limit for the 0.4–1 MeV flux of $1.5 \times 10^{-9} \text{ erg cm}^{-2} \text{ s}^{-1}$.

4.2.3. Soft State

In the soft state the soft X-ray spectrum below 10 keV is dominated by a ~ 1 keV accretion disk. This disk, however, does not influence the >10 keV spectrum studied here. A single power law gives a poor representation of the broad band spectrum ($\chi^2_\nu = 6.0$ for 77 dof). The JEM-X and ISGRI spectra are particularly discrepant and a possible hint for a high energy roll-over is seen in the residuals. A cutoff power law greatly improves the fit statistics ($\chi^2_\nu = 1.68$ for 75 dof), but the modeling is still not satisfactory and the JEM-X normalization constants are inconsistent with the detector calibration uncertainty. Residuals in the 15–50 keV range suggest that reflection on the accretion disk may occur. Adding the `reflect` model improves the fit to $\chi^2_\nu = 1.24$ (74 dof). The normalization constant for the JEM-X1 detector has to be forced to be above 0.85 as it would naturally converge to about 0.8. Alternatively describing the data with a simple reflected power law without a cutoff results in $\chi^2_\nu = 1.88$ (76 dof) and shows that the cutoff is genuinely present. The chance improvement from a reflected power-law spectrum to a reflected cutoff power-law spectrum is about 4×10^{-8} according to an F-test. Replacing the phenomenological model with a Comptonization continuum that is modified by reflection yields $\chi^2_\nu = 1.69$ (75 dof, Table 1).

The >400 keV data were then added. Since the Compton mode spectrum has a very low statistical quality and in order not to increase the number of degeneracies, we fixed its

¹⁴ The choice of a higher seed photon temperature in the IS does not influence the >10 keV spectrum and was only motivated by the desire to be consistent with the expectation of a hotter disk in the IS.

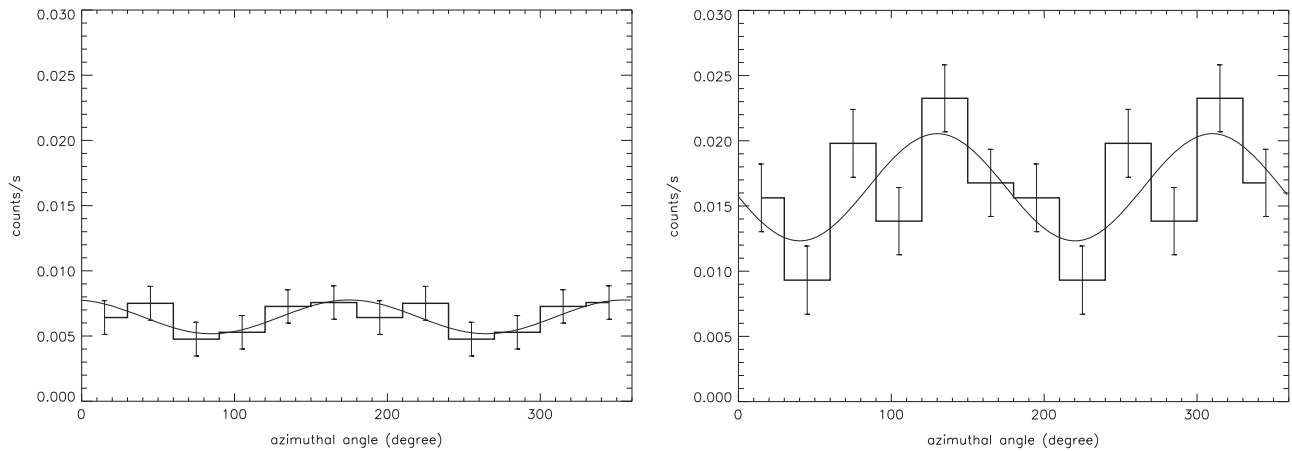


Figure 4. Polarigrams obtained in the LHS. Left: 300–400 keV. Right: 400–2000 keV.

constant to a value of one. The `reflect*comptt` model is still statistically acceptable, and only the highest spectral bin (550–2000 keV) indicates an excess of source photons compared to the model ($\chi^2_\nu = 1.76$, 77 dof). Adding a power-law component to the overall spectrum improves the modeling of the spectrum to $\chi^2_\nu = 1.69$ (75 dof), but if left free to vary Γ is completely unconstrained. We fix it at 1.6 ($\chi^2_\nu = 1.70$, 76 dof, 0.11 chance probability according to the F-test) and derive a 3σ upper limit of 0.93×10^{-9} erg cm $^{-2}$ s $^{-1}$ for the 0.4–1 MeV flux.

4.3. State Resolved Polarization Analysis

Polarigrams were obtained for each of the three spectral states. The low statistics of the IS (the source significance in the Compton mode is 5.7σ) does not permit us to constrain the 250–3000 keV polarization fraction.

In the HSS, the detection significances of Cyg X-1 with the Compton mode are 4.2σ and 7.7σ in the 300–400 keV and 400–2000 keV bands respectively. A weighted least square fit procedure was used to fit the polarigrams. A constant represents the 400–2000 keV polarigram rather well ($\chi^2_\nu = 1.6$, 5 dof, not shown). The 1σ upper limit of the 400–2000 keV polarization fraction in the HSS is $\sim 70\%$.

Figure 4 shows the LHS polarigrams in two energy ranges: 300–400 keV and 400–2000 keV. Note that the data selection described in Section 3 is at the origin of the different count rates between the polarigrams shown here and those in Figure 2 or LRW11. This effect is more obvious at the highest energies where the different spectral slopes have the largest impact (Figure 3). In the lower energy range, the Compton mode detection significance of Cyg X-1 is 12.3σ . The polarigram can be described by a constant ($\chi^2_\nu = 0.87$, 5 dof). We estimate an upper limit for the polarization fraction of $\Pi_{300-400 \text{ keV, LHS}} = 22\%$ in this energy range. The 400–2000 keV energy range polarigram shows clear deviation from a constant and a constant poorly represents the data ($\chi^2_\nu = 3.5$, 5 dof). The pattern and fit indicate that the photons scattered in ISGRI are not evenly distributed in angle, but that the scattering has a preferential angle as is expected from a polarized signal (Section 2.2). We describe the distribution of the polarigram with the expression of Equation (2) and obtain the values of the parameters a_0 and ϕ_0 with a least square technique. The fit is better than that to a constant, although not formally good

($\chi^2_\nu = 2.0$, 3 dof) due to the low value of the periodogram at azimuthal angle 100° (Figure 4). Assuming that the non constancy of the polarigram is evidence for a real polarized signal (an assumption also consistent with the independent detections of polarized emission in Cygnus X-1 with SPI; Jourdain et al. 2012), we estimate that the polarization fraction is $\gtrsim 10\%$ at the 95% level, and greater than a few % at the 99.7% level. In other words we obtain a significance higher than 3σ for a polarized 400–2000 keV LHS emission. We determine a polarization fraction and a credibility interval of $\Pi_{400-2000 \text{ keV, LHS}} = 75\% \pm 32\%$ at position angle $\text{PA}_{\text{Cyg X-1, LHS}} = 40^\circ \pm 14^\circ.3$. The values of the polarization fraction and angle are consistent with those found by JRC12. We note that an error of 180° in the angle convention in LRW11 led to $\text{PA} = 140^\circ$, which after correction becomes 40° , in agreement with our state resolved result (see also JRC12). Note that the good agreement of our results with those obtained with SPI in the case of Cyg X-1, and also the fact that IBIS also detected polarization in the high energy emission of the Crab Nebula and pulsar (Forot et al. 2008) at values compatible with those obtained with SPI (Dean et al. 2008), increase the confidence in the reality and validity of our results.

5. DISCUSSION AND CONCLUSIONS

5.1. The ≥ 400 keV Hard Tail

Our analysis shows that the >400 keV spectral properties of Cyg X-1 depend on the spectral state, as already suggested previously (e.g., McConnell et al. 2002). We detect a strong hard tail in the LHS, but obtain only upper limits in the IS and HSS. In Figure 5 (left), we show a comparison of our LHS 0.75–1 MeV spectrum with those obtained with *Compton Gamma Ray Observatory*/COMPTEL during the 1996 June HSS and during an extended LHS observed with this instrument (McConnell et al. 2000, 2002). The IBIS hard tail is compatible in terms of fluxes to within 2σ to those seen with COMPTEL and also with the *INTEGRAL*/SPI hard tail reported in JRC12 (see their Figure 5). It is worth noting that Cyg X-1 is a notoriously highly variable source and flux evolution between different epochs is expected. To illustrate this behavior, we study data taken during two main periods, that covering 2003 March–2007 December (MJD 52722–54460) and 2008 March–2009 December (MJD 54530–55196), respectively.

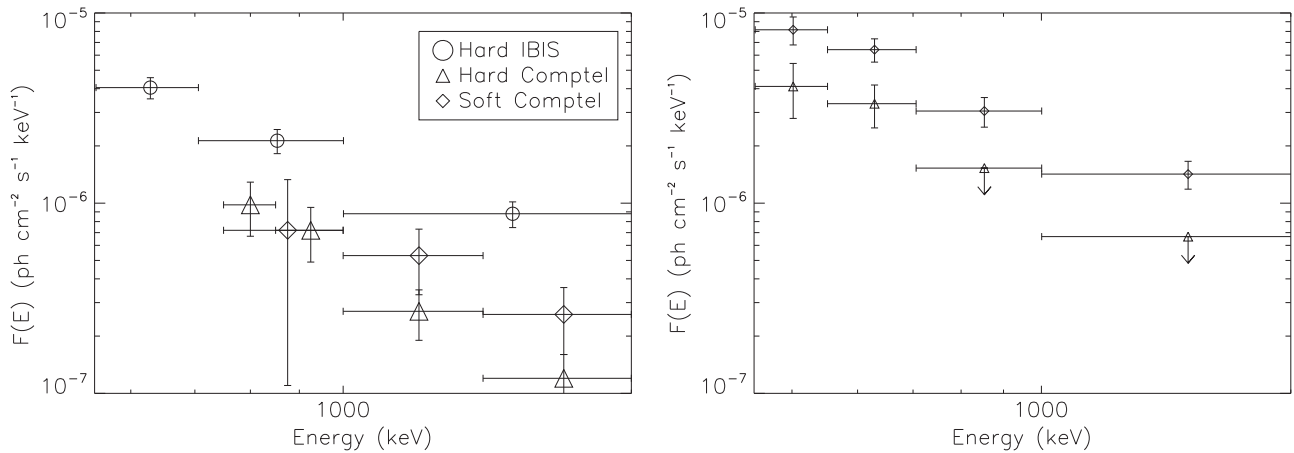


Figure 5. Left: comparison of the *INTEGRAL*/IBIS and *CGRO*/Comptel high energy spectra. Right: comparison of the *INTEGRAL*/Compton spectra accumulated over two different epochs.

These intervals correspond to the analysis of [LRW11](#). The two Compton spectra are shown in Figure 5 (right). It is obvious that the flux of the hard tail varied between the two epochs and an evolution of the slope may also be visible. We note that these data are not separated by states, but as they cover the period before 2009 December, they are dominated by the LHS (e.g., Figure 1). We therefore conclude that, even in the same state, the hard tail shows luminosity variations.

A major difference from McConnell et al. (2002) is the non-detection of a hard tail in the HSS. McConnell et al. (2002) remark that between two epochs of HSS the hard tail either has a higher flux than in their averaged LHS or is not detected. Malyshev et al. (2013) also note that the 1996 HSS hard tail comes from a single occurrence of this state and may not reflect typical behavior. While detection of a hard tail during the LHS, even if it shows variations, indicates an underlying process that is rather stable over long periods of time, the apparent transience of the HSS hard tail may indicate a different origin for this feature. For example, in Cyg X-3 the very high energy (Fermi) flares are associated with transitions to the ultra soft state (Fermi LAT Collaboration et al. 2009). While this is similar to what is seen in Cyg X-1, all Fermi γ -ray flares of Cyg X-1 were reported during the LHS (Bodaghee et al. 2013; Malyshev et al. 2013). While the lack of simultaneous very high energy GeV–TeV data and/or polarimetric studies of the Comptel HSS hard tail prevent any further conclusion on the origin of this component, we conclude that the HSS hard tail and the LHS hard tail could be of different origins.

5.2. Polarization of the Hard Tail and its Possible Origin

A clear polarized signal is detected from Cyg X-1 with both IBIS and SPI while accumulating all data regardless of the spectral state of the source ([LRW11](#), [JRC12](#)). Here we separated the data into different spectral states and studied the state dependent high energy polarization properties. The HSS and 300–400 keV polarigram can be described by a constant, indicating no or very small levels of polarization. The 400–2000 keV LHS polarigram shows a large deviation from a constant, which indicates that the Compton scattering from ISGRI is not an evenly circular distribution on PICSiT. We interpret this as evidence for the presence of polarization in this energy range, even if the polarigram shows some deviations from the theoretically expected curve (Figure 4). In the

300–400 keV range, no evidence for polarization is found. This is consistent with the results obtained with SPI ([JRC12](#)) and shows that the polarization fraction is strongly energy dependent. Assuming a non-null level of polarization, a reasonable assumption given the above arguments, we estimate that the detection of polarized emission is significant at higher than 3σ . Given the larger amount of data and the separation into different spectral states, one could have expected to obtain more robust results and more constrained polarization parameters compared to [LRW11](#) and [JRC12](#), while the uncertainties we obtained are, at best, of the same order. The reason for this lies in the behavior of Cyg X-1. While the earlier studies did not perform a state dependent analysis, our state classification reveals that both studies were dominated by data taken during the LHS and the IS (see also Figure 1). In fact, compared to [LRW11](#) the number of ScWs measured during the LHS increased only by 13%, and 75% of the IS data comes from the period considered in these earlier studies, i.e., before \sim MJD 55200. On the other hand, about 94% of the HSS data are new. It is therefore not surprising that our hard state result is consistent with the earlier results, as these were fully dominated by the (polarized) hard state data. The exposure of the less polarized IS data was not large enough to significantly “dilute” the polarization. Our result clearly shows that larger amounts of data in each of the states are needed to refine the constraint on the polarization properties and their relation to the spectral states.

Our LHS spectral analysis shows that the 10–1000 keV spectrum can be decomposed into several spectral components: a (reflected) thermal Comptonization component in the range \sim 10–400 keV, and a power-law tail dominating above \sim 400 keV (Section 4.2.1). The origin of the seed photons for the Compton component may either be an accretion disk or synchrotron photons from a compact jet undergoing synchrotron self-Comptonization (SSC). As discussed elsewhere (e.g., Laurent et al. 2011), due to the large number of scatterings the Comptonization spectrum from a medium with an optical depth $\tau \geq 1$ is not expected to show intrinsic polarization, especially with such a high fraction as the one we detect here. Multiple Compton scattering, as expected in such a medium, will “wash out” the polarization of the incident photons even if the seed photons are polarized (e.g., jet photons). It is therefore not surprising that the LHS \lesssim 400 keV component has a very low

(or zero) polarization fraction (see also Russell & Shahbaz 2013).

The origin of the hard-MeV tail is much less clear and is highly model-dependent. Two main families of models can explain the (co-)existence of cutoff power-law and/or pure power-law like emissions in the energy spectra of BHBs. The first is based on the presence of a hybrid thermal–non thermal population of electrons in a “corona,” and hybrid Comptonization has been successfully applied to the spectra of, e.g., GRO J1655–40 or GX 339–4 (e.g., Joinet et al. 2007; Caballero-García et al. 2009), and even to ~ 1 –10000 keV spectra of Cyg X-1, in both the HSS and LHS (McConnell et al. 2002). A double thermal component has been used to represent the 20–1000 keV SPI data of 1E 1740–2947 well (Bouchet et al. 2009).

The second family of models essentially contains the same radiation processes but is based on the presence of a jet emitting through direct synchrotron emission, thermal Comptonization of the soft disk photons on the base of the jet, and/or SSC of the synchrotron photons by the jet’s electrons (e.g., Markoff et al. 2005). Such models have been used with success to fit the data of some BHs, and particularly GX 339–4 and XTE J1118+480 (Markoff et al. 2005; Maitra et al. 2009; Nowak et al. 2011). It should be noted, however, that they obviously rely on the presence of a compact jet and therefore can only be valid when/if a compact jet is present.

The capacities of the current high energy missions, albeit excellent, do not permit an easy discrimination between the different families of models. This has been nicely illustrated in the specific case of Cyg X-1 through the 0.8–300 keV spectral analysis of the Suzaku/RXTE observations (Nowak et al. 2011). Different and complementary approaches and arguments can, however, be used to try and identify the most likely origin for the hard power-law tail. The fundamental plane between radio luminosity and X-ray luminosity (e.g., Corbel et al. 2003) was originally used as an argument for a (small) contribution of the jet to the X-ray domain. Our approach here was to first separate the radio data sets into different spectral states, based on a model-independent classification. It was only because of this separation that we could show that a hard polarized tail is present in the LHS, with a high polarization fraction, together with a radio jet. The very high level of polarization can only originate from optically thin synchrotron emission (see below), and implies a highly ordered magnetic field similar to that expected in jets. The synchrotron tail coincides with thermal Comptonization at lower energies and with a radio jet. The presence of all these features is qualitatively compatible with the multi-component emission processes predicted by compact jet models such as those of Markoff et al. (2005). While polarization of the (compact) jet emission has already been widely reported in the radio domain (Brocksopp et al. 2013, and references therein), a thorough study of the multi-wavelength polarization properties of Cyg X-1 has only recently been undertaken by Russell & Shahbaz (2013). These authors, in particular, showed that the multi-wavelength spectrum and polarization properties of Cyg X-1 are quantitatively compatible with the presence of a compact jet that dominates the radio to IR domain and is also responsible for the MeV tail. A similar conclusion was drawn by Malyshev et al. (2013) under the assumption that “the polarization measurements were robust” and that therefore the MeV tail could only originate from synchrotron emission. This pre-

requisite is reinforced by our refined and spectral-state dependent study of the polarized properties of Cyg X-1 at 0.3–1 MeV. A polarized signal is indeed suggested by the 400–2000 keV LHS data and the large degree of polarization measured in Section 4.3 implies a very ordered magnetic field. Assuming the magnetic field lines are anchored in the disk implies that the γ -ray polarized emission comes from close to the inner ridge of the disk where the magnetic energy density is highest. This constraint is difficult to reconcile with a spherically shaped corona medium, where the magnetic field lines are more likely to be tangled and where the polarized component necessarily comes from the outer shells of the corona where the optical depth is the lowest. We therefore conclude that in the LHS the 0.4–2 MeV tail detected with *INTEGRAL*/IBIS is very likely due to optically thin synchrotron emission, and that this emission comes from the detected compact jet.

5.3. Compatibility of the Cyg X-1 Hard State Parameters with Synchrotron Emission

The synchrotron spectrum of a population of electrons following a power-law distribution, $dN(E) \propto E^{-p}d(E)$, where p is the particle distribution index, can be approximated by a power-law function over a limited range of energy, i.e., $F_{E_1, E_2}(E) \propto E^{-\alpha}$ over $[E_1, E_2]$ (Rybicki & Lightman 1979). In the case of compact jets, two main domains are usually considered: the optically thick regime with $\alpha \lesssim 0$ and the optically thin regime with $\alpha > 0$. The break between the two regimes is typically in the infrared band (e.g., Corbel & Fender 2002; Rahoui et al. 2011; Corbel et al. 2013; Russell & Shahbaz 2013). The jet synchrotron spectrum is optically thin toward higher energies, and here $\alpha = (p - 1)/2$. The jet emission becomes negligible in the range from the optical to hard X-rays when compared to the contribution from other components such as the companion star, the accretion disk, or the corona. Our results indicate that it again dominates above a few hundred keV (see also Russell & Shahbaz 2013, for a multi-components modeling of the multi-wavelength Cyg X-1 spectrum).

The degree of polarized emission expected in the optically thin regime is $\Pi = \frac{p+1}{p+7/3}$ (Rybicki & Lightman 1979). Since the flux spectral index $\alpha = \Gamma - 1$, where Γ is the photon spectral index, it is possible to deduce p from the measured spectral shape. With $\Gamma = 1.4^{+0.2}_{-0.3}$ (Section 4.2.1) we obtain $p = 1.8^{+0.4}_{-0.7}$ and thus expect $\Pi_{\text{expected}} = 67.8^{+2.7}_{-5.5}\%$. This value is consistent with the value measured in the LHS ($\Pi = 75\% \pm 32\%$).

We determine a polarization angle of $\sim 40^\circ$ compatible with the SPI results (JRC12). This angle, however, differs by about 60° from the polarization angles measured in the radio and optical (Russell & Shahbaz 2013, and references therein). Assuming that the γ -ray polarized component comes from the region of the jet that is closest to the launch site (i.e., the inner ridge of the disk and/or the BH), the change in polarization angle implies that the field lines in the γ -ray emitting region have a different orientation than farther out in the jet. This could be indicative of a relatively large opening angle at the basis of the jet (as sketched in Figure 3 of Russell & Shahbaz 2013). Alternatively the large offset could simply be due to strongly twisted magnetic field lines close to the accretion disk.

6. SUMMARY

We have presented a broad band 10 keV–2 MeV spectral analysis of the microquasar Cyg X-1 based on about 10 years of data collected with the JEM-X and IBIS telescopes on board the *INTEGRAL* observatory. We have used the classification criteria of Grinberg et al. (2013) to separate the data into hard (LHS), intermediate (IS), and soft (HSS) states. We have studied the radio behavior of the source associated with these states as observed with the Ryle/AMI radio telescope at 15 GHz.

1. The ≤ 400 keV emission is well represented by Comptonization spectra with further reflection off the accretion disk. In the LHS and IS, the Comptonization process is thermal and optically thick, i.e., the corona has an optical depth $\tau > 1$ and the electrons have a Maxwellian distribution. As a result, a clear high-energy cutoff is seen in the spectra. In the HSS the situation is not that clear, although a cutoff is also necessary to give a good representation of the broad band spectrum.
2. A clear hard tail is detected in the LHS when also considering the 0.4–2 MeV data. This high energy component is well represented by a hard power law with no obvious cutoff. The detection of the hard tail is compatible with earlier claims of the presence of such a component in spectra of Cyg X-1. We show that this component is variable within same state, as is seen when considering *INTEGRAL* observations from two arbitrary epochs but the same state.
3. In the radio domain, the 15 GHz data show a definite detection with averaged flux densities of respectively ~ 13 and ~ 15 mJy in the LHS and IS, compatible with the presence of a compact jet in those states. No persistent radio emission is detected in the HSS, implying the absence of a compact radio core.
4. In the LHS, we measure a polarized signal above 400 keV with a large polarization fraction ($75\% \pm 32\%$). This high degree of polarization and the polarization angle ($40^\circ \pm 14^\circ$) are both compatible with previous studies by us and others. We obtain non-constraining upper limits on the polarization fraction in the IS and HSS, which have significantly lower exposure.
5. The high degree of polarization of the hard tail can only originate from synchrotron emission in a highly ordered magnetic field. The demonstrated presence of radio emission in the LHS points toward the compact jet as the origin for the 0.4–2 MeV emission, corroborating earlier theoretical and multi-wavelengths studies (Malyshch et al. 2013; Russell & Shahbaz 2013). Our spectral state-resolved and multi-wavelength approach therefore further confirms the conclusion presented in the earlier, non state-resolved studies based on *INTEGRAL* data only (Laurent et al. 2011; Jourdain et al. 2012).
6. We increased the total *INTEGRAL* exposure time and, in particular, nearly doubled the amount of data taken in the HSS. We, however, still do not reach strong constraints on the polarization fraction in this state, even if we showed that the hard tail is much fainter. Provided the source does not change state, we have gotten *INTEGRAL* time approved to further increase the exposure time in the HSS, which will allow us to obtain tighter constraints on the polarization signal in this very state.

This paper is based on observations with *INTEGRAL*, an ESA project with instruments and a science data center funded by ESA member states (especially the PI countries: Denmark, France, Germany, Italy, Switzerland, Spain) and with the participation of Russia and the USA. We acknowledge S. Corbel, R. Belmont, J. Chenevez, and J. A. Tomsick for very fruitful discussions about several aspects presented in this paper. J.R. acknowledges funding support from the French Research National Agency: CHAOS project ANR-12-BS05-0009 (<http://www.chaos-project.fr>), and from the UnivEarthS Labex program of Sorbonne Paris Cité (ANR-10-LABX-0023 and ANR-11-IDEX-0005-02). This work has been partially funded by the Bundesministerium für Wirtschaft und Technologie under Deutsches Zentrum für Luft- und Raumfahrt Grants 50 OR 1007 and 50 OR 1411. V.G. acknowledges support provided by NASA through the Smithsonian Astrophysical Observatory (SAO) contract SV3-73016 to MIT for Support of the Chandra X-ray Center (CXC) and Science Instruments; CXC is operated by SAO for and on behalf of NASA under contract NAS8-03060. We acknowledge the support by the DFG Cluster of Excellence “Origin and Structure of the Universe.” We are grateful for the support of M. Cadolle Bel through the Computational Center for Particle and Astrophysics (C2PAP).

REFERENCES

- Arnaud, K. A. 1996, in ASP Conf. Ser. 101, *Astronomical Data Analysis Software and Systems V*, ed. G. H. Jacoby & J. Barnes (San Francisco, CA: ASP), 17
- Böck, M., Grinberg, V., Pottschmidt, K., et al. 2011, *A&A*, **533**, A8
- Bodaghee, A., Tomsick, J. A., Pottschmidt, K., et al. 2013, *ApJ*, **775**, 98
- Bolton, C. T. 1972, *Natur*, **235**, 271
- Bolton, C. T. 1975, *ApJ*, **200**, 269
- Bouchet, L., del Santo, M., Jourdain, E., et al. 2009, *ApJ*, **693**, 1871
- Bowyer, S., Byram, E. T., Chubb, T. A., & Friedman, H. 1965, *Sci*, **147**, 394
- Brocksopp, C., Corbel, S., Tzioumis, A., et al. 2013, *MNRAS*, **432**, 931
- Brocksopp, C., Tarasov, A. E., Lyuty, V. M., & Roche, P. 1999, *A&A*, **343**, 861
- Caballero, I., Zurita Heras, J. A., Mattana, F., et al. 2012, in Proc. of An *INTEGRAL* View of the High-energy Sky (the First 10 Years), **142** (<http://pos.sissa.it/cgi-bin/reader/conf.cgi?confid=176>)
- Caballero-García, M. D., Miller, J. M., Trigo, M. D., et al. 2009, *ApJ*, **692**, 1339
- Cadolle Bel, M., Sizun, P., Goldwurm, A., et al. 2006, *A&A*, **446**, 591
- Corbel, S., Aussel, H., Broderick, J. W., et al. 2013, *MNRAS*, **431**, L107
- Corbel, S., & Fender, R. P. 2002, *ApJL*, **573**, L35
- Corbel, S., Fender, R. P., Tomsick, J. A., Tzioumis, A. K., & Tingay, S. 2004, *ApJ*, **617**, 1272
- Corbel, S., Nowak, M. A., Fender, R. P., Tzioumis, A. K., & Markoff, S. 2003, *A&A*, **400**, 1007
- Coriat, M., Corbel, S., Prat, L., et al. 2011, *MNRAS*, **414**, 677
- Dean, A. J., Clark, D. J., Stephen, J. B., et al. 2008, *Sci*, **321**, 1183
- Fender, R., Corbel, S., Tzioumis, T., et al. 1999, *ApJL*, **519**, L165
- Fender, R. P., Homan, J., & Belloni, T. M. 2009, *MNRAS*, **396**, 1370
- Fender, R. P., Stirling, A. M., Spencer, R. E., et al. 2006, *MNRAS*, **369**, 603
- Fermi LAT Collaboration, Abdo, A. A., Ackermann, M., et al. 2009, *Sci*, **326**, 1512
- Forot, M., Laurent, P., Grenier, I. A., Gouffès, C., & Lebrun, F. 2008, *ApJL*, **688**, L29
- Gallo, E., Fender, R. P., & Pooley, G. G. 2003, *MNRAS*, **344**, 60
- García, J., Dauser, T., Lohfink, A., et al. 2014, *ApJ*, **782**, 76
- Gies, D. R., Bolton, C. T., Thomson, J. R., et al. 2003, *ApJ*, **583**, 424
- Grinberg, V., Hell, N., Pottschmidt, K., et al. 2013, *A&A*, **554**, A88
- Grinberg, V., Leutenegger, M. A., Hell, N., et al. 2015, *A&A*, **576**, A117
- Grinberg, V., Pottschmidt, K., Böck, M., et al. 2014, *A&A*, **565**, A1
- Homan, J., & Belloni, T. 2005, *ApSS*, **300**, 107
- Joinet, A., Jourdain, E., Malzac, J., et al. 2007, *ApJ*, **657**, 400
- Jourdain, E., Roques, J. P., Chauvin, M., & Clark, D. J. 2012, *ApJ*, **761**, 27
- Labanti, C., di Cocco, G., Ferro, G., et al. 2003, *A&A*, **411**, L149
- Laurent, P., Rodriguez, J., Wilms, J., et al. 2011, *Sci*, **332**, 438

- Lebrun, F., Leray, J. P., Lavocat, P., et al. 2003, *A&A*, **411**, L141
- Lei, F., Dean, A. J., & Hills, G. L. 1997, *SSRv*, **82**, 309
- Lund, N., Budtz-Jørgensen, C., Westergaard, N. J., et al. 2003, *A&A*, **411**, L231
- Maier, D., Tenzer, C., & Santangelo, A. 2014, *PASP*, **126**, 459
- Maitra, D., Markoff, S., Brocksopp, C., et al. 2009, *MNRAS*, **398**, 1638
- Malyshev, D., Zdziarski, A. A., & Chernyakova, M. 2013, *MNRAS*, **434**, 2380
- Markoff, S., Nowak, M. A., & Wilms, J. 2005, *ApJ*, **635**, 1203
- McConnell, M. L., Ryan, J. M., Collmar, W., et al. 2000, *ApJ*, **543**, 928
- McConnell, M. L., Zdziarski, A. A., Bennett, K., et al. 2002, *ApJ*, **572**, 984
- Nowak, M. A., Hanke, M., Trowbridge, S. N., et al. 2011, *ApJ*, **728**, 13
- Orosz, J. A., McClintock, J. E., Aufdenberg, J. P., et al. 2011, *ApJ*, **742**, 84
- Pooley, G. G., & Fender, R. P. 1997, *MNRAS*, **292**, 925
- Pottschmidt, K., Wilms, J., Chernyakova, M., et al. 2003a, *A&A*, **411**, L383
- Pottschmidt, K., Wilms, J., Nowak, M. A., et al. 2003b, *A&A*, **407**, 1039
- Quinn, J. L. 2012, *A&A*, **538**, A65
- Rahoui, F., Lee, J. C., Heinz, S., et al. 2011, *ApJ*, **736**, 63
- Reid, M. J., McClintock, J. E., Narayan, R., et al. 2011, *ApJ*, **742**, 83
- Remillard, R. A., & McClintock, J. E. 2006, *ARA&A*, **44**, 49
- Reynolds, M. T., & Miller, J. M. 2013, *ApJ*, **769**, 16
- Rodriguez, J., Hannikainen, D. C., Shaw, S. E., et al. 2008a, *ApJ*, **675**, 1436
- Rodriguez, J., Shaw, S. E., Hannikainen, D. C., et al. 2008b, *ApJ*, **675**, 1449
- Russell, D. M., & Shahbaz, T. 2013, *MNRAS*, in press, arXiv:1312.0942
- Rybicki, G. B., & Lightman, A. P. 1979, *AstQ*, **3**, 199
- Stirling, A. M., Spencer, R. E., de la Force, C. J., et al. 2001, *MNRAS*, **327**, 1273
- Titarchuk, L. 1994, *ApJ*, **434**, 570
- Titarchuk, L., & Hua, X.-M. 1995, *ApJ*, **452**, 226
- Titarchuk, L., & Lyubarskij, Y. 1995, *ApJ*, **450**, 876
- Ubertini, P., Lebrun, F., Di Cocco, G., et al. 2003, *A&A*, **411**, L131
- Vaillancourt, J. E. 2006, *PASP*, **118**, 1340
- Varnière, P., Tagger, M., & Rodriguez, J. 2011, *A&A*, **525**, A87
- Varnière, P., Tagger, M., & Rodriguez, J. 2012, *A&A*, **545**, A40
- Vedrenne, G., Roques, J.-P., Schönfelder, V., et al. 2003, *A&A*, **411**, L63
- Walborn, N. R. 1973, *ApJL*, **179**, L123
- Webster, B. L., & Murdin, P. 1972, *Natur*, **235**, 37
- Wilms, J., Nowak, M. A., Pottschmidt, K., Pooley, G. G., & Fritz, S. 2006, *A&A*, **447**, 245
- Wilms, J., Pottschmidt, K., Pooley, G. G., et al. 2007, *ApJL*, **663**, L97
- Xiang, J., Lee, J. C., Nowak, M. A., & Wilms, J. 2011, *ApJ*, **738**, 78
- Ziółkowski, J. 2014, *MNRAS*, **440**, L61